High-Relaxivity Superparamagnetic Iron Oxide Nanoworms with Decreased Immune Recognition and Long-Circulating Properties

Guankui Wang,[†] Swetha Inturi,[†] Natalie J. Serkova,[‡] Sergey Merkulov,[§] Keith McCrae,[§] Stephen E. Russek,[‖] Nirmal K. Banda,[⊥] and Dmitri Simberg*[,†]

[†]The Skaggs School of Pharmacy and Pharmaceutical Sciences, University of Colorado Denver, Anschutz Medical Campus, 12850 E. Montview Boulevard, Aurora, Colorado 80045, United States, [‡]Department of Anesthesiology, School of Medicine, University of Colorado Denver, Anschutz Medical Campus, 12631 E 17th Place, Aurora, Colorado 80045, United States, [§]Department of Cellular and Molecular Medicine, Cleveland Clinic Lerner Research Institute, 9500 Euclid Avenue, Cleveland, Ohio 44195, United States, [‖]Biomagnetic Imaging Standards and Microsystems, National Institute of Standards and Technology (NIST), 325 Broadway St., Boulder, Colorado 80305, United States, and [⊥]Division of Rheumatology, School of Medicine, University of Colorado Denver, Anschutz Medical Campus, 1775 Aurora Court, Aurora, Colorado 80045, United States

ABSTRACT One of the core issues of nanotechnology involves masking the foreignness of nanomaterials to enable *in vivo* longevity and long-term immune evasion. Dextran-coated superparamagnetic iron oxide nanoparticles are very effective magnetic resonance imaging (MRI) contrast agents, and strategies to prevent immune recognition are critical for their clinical translation. Here we prepared 20 kDa dextran-coated SPIO nanoworms (NWs) of 250 nm diameter and a high molar transverse relaxivity rate R_2 ($\sim$400 mM^{-1} s^{-1}) to study the effect of cross-linking-hydrogelation with 1-chloro-2,3-epoxypropane (epichlorohydrin) on the immune evasion both *in vitro* and *in vivo*. Cross-linking was performed in the presence of different concentrations of NaOH (0.5 to 10 N) and different temperatures (23 and 37 °C). Increasing NaOH concentration and temperature significantly decrease the binding of anti-dextran antibody and dextran-binding lectin conconavalin A to the NWs. The decrease in dextran immunoreactivity correlated with the decrease in opsonization by complement component 3 (C3) and with the decrease in the binding of the lectin pathway factor MASP-2 in mouse serum, suggesting that cross-linking blocks the lectin pathway of complement. The decrease in C3 opsonization correlated with the decrease in NW uptake by murine peritoneal macrophages. Optimized NWs demonstrated up to 10 h circulation half-life in mice and minimal uptake by the liver, while maintaining the large 250 nm size in the blood. We demonstrate that immune recognition of large iron oxide nanoparticles can be efficiently blocked by chemical cross-linking-hydrogelation, which is a promising strategy to improve safety and bioinertness of MRI contrast agents.

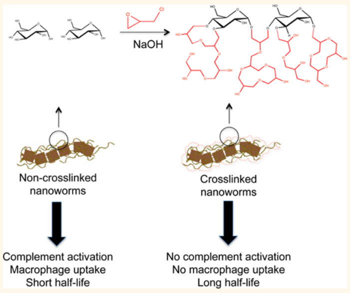

KEYWORDS: iron oxide · dextran · nanoworms · cross-linking · epichlorohydrin · blood circulation · magnetic resonance imaging · complement activation · component 3

Due to excellent anatomical resolution and contrast, magnetic resonance imaging (MRI) is increasingly being used as a first-choice clinical imaging modality. Superparamagnetic iron oxide (SPIO) nanoparticles are potent clinically approved MRI contrast agents that cause shortening of transverse (T_2) proton relaxation times, resulting in dark negative contrast areas of T_2-weighted MR images.[1] All clinically approved SPIO contrast agents are synthesized using the one-pot procedure described by Molday and MacKenzie,[2] wherein Fe^{2+} and Fe^{3+} salts are mixed with a biopolymer (usually dextran or carboxydextran) and neutralized with ammonia. Resulting SPIO consists of magnetite–maghemite (Fe_3O_4 and γ-Fe_2O_3) crystals embedded in a meshwork of the polysaccharide. The surface of iron oxide crystals is mostly acidic due to hydration of Fe^{3+},[3,4] leading to hydrogen bonding with hydroxyl groups of the polysaccharide coating. The coatings are critical to impart water solubility and colloidal stability to the particles. The key advantages of Molday precipitation include easy and scalable fabrication and the low cost of polysaccharides used for the

* Address correspondence to Dmitri.Simberg@ucdenver.edu.

Received for review September 11, 2014 and accepted November 24, 2014.

10.1021/nn505126b

synthesis. The main disadvantages of the resulting SPIO nanoparticles are immune-related adverse effects in patients, fast clearance, and nonspecific uptake by monocytes and macrophages.[5−8] The unfavorable pharmacokinetics precludes the use of SPIO for imaging of organs and tissues outside macrophage-rich organs (liver and spleen).[9]

Recently, cross-linked iron oxide (CLIO) nanoparticles have been described. CLIO was prepared by cross-linking ultrasmall (15−30 nm) monocrystalline SPIO with 1-chloro-2,3-epoxypropane (epichlorohydrin) in the presence of NaOH. CLIO had a very low transverse relaxivity rate R_2 of ∼60 $\text{mM}^{-1}\ \text{s}^{-1}$ and ultrasmall size and, due to long-circulating properties, became a popular nanoplatform for imaging applications.[10,11] More recently, Sailor's group described a synthesis of larger CLIOs dubbed magnetic nanoworms (NWs) with a hydrodynamic diameter of 60 nm, moderate R_2 relaxivity of 100−160 $\text{mM}^{-1}\ \text{s}^{-1}$, and saturation magnetization of ∼80 emu/g.[12,13] CLIO NWs proved to be a useful platform as multifunctional sensors and drug delivery.[14−18]

While there is a definite need for ultrasmall iron oxides due to their efficient tissue penetration and macrophage evasion, the disadvantage of the ultrasmall SPIO nanoparticles is their relatively low magnetic contrast properties (relaxivity). Transverse relaxivity of larger iron oxides is higher because of aggregated core and low polymer/core ratio,[19−24] and their cell uptake is generally more efficient than ultrasmall nanoparticles.[5,25−28] To achieve specific and sensitive imaging of disease markers, nanoparticles that possess good contrast properties, avoid immune recognition, and have sufficient circulation time need to be developed.[9,19,29−31] Here we synthesized large, 250 nm diameter SPIO NWs with high transverse relaxivity R_2 of ∼400 $\text{mM}^{-1}\ \text{s}^{-1}$ and tested the effect of cross-linking with epichlorohydrin on R_2 relaxivity and immune recognition *in vitro* and *in vivo*. Epichlorohydrin cross-linking has been empirically found to prolong circulation time and to prevent liver macrophage recognition of smaller CLIO,[32] but the effect of cross-linking conditions on the size, R_2 relaxivity, and immune recognition of larger nanoparticles is unknown.[33,34] We demonstrate that increasing NaOH concentration and temperature blocks dextran immunoreactivity, prevents activation of sugar-dependent pathways of complement in mouse sera, and reduces recognition by macrophages *in vitro* and clearance by Kupffer cells *in vivo*. Surprisingly, we also demonstrate that 250 nm cross-linked NWs are able to circulate in blood with up to a 10 h half-life. These findings bear important implications on the rational design of bioinert iron oxides for cell labeling, cell isolation, and *in vivo* molecular imaging.

RESULTS AND DISCUSSION

Synthesis and Characterization of Iron Oxide Nanoworms. SPIO NWs were synthesized by a one-pot ammonia precipitation reaction of Fe^{2+} and Fe^{3+} in the presence of nonreduced dextran (15−25 kDa). Following the synthesis, NWs were cross-linked with epichlorohydrin (ECH) in the presence of NaOH. ECH reacts with sugar hydroxyls (*via* chloride or epoxide), resulting in etherification and cross-linking (Figure 1A). The methylating and cross-linking effect of epichlorohydrin[35] results in the formation of a cross-linked dextran hydrogel,[33] and concentration of NaOH and temperature of the reaction are critical for the hydrogel formation. In order to systematically study the effects of cross-linking conditions on size, relaxivity, and immunological properties of SPIO, the following protocol was used (Figure 1B; see Materials and Methods). For "mild cross-linking", SPIO was reacted with ECH using different concentrations of NaOH solutions (0.5, 2.5, 5, and 10 N), at 30 rpm mixing speed and 23 °C. For "harsh cross-linking", all NWs after the mild cross-linking were cross-linked using 10 N NaOH, at 1400 rpm mixing speed and 37 °C. Thereafter, we refer to mild cross-linked iron oxide as CLIO-M (with the NaOH normality in parentheses) and harsh cross-linked SPIO as CLIO-H (with the NaOH normality in the previous step in parentheses). Note that NaOH concentrations in parentheses are not the final concentration in the reaction, but rather the concentration of NaOH added to the reaction (see Materials and Methods), so the resulting concentration was about one-third of that (ECH is not miscible with water, so its volume is not considered). The reason for not subjecting SPIO directly to a harsh cross-linking step was that, without the mild pre-cross-linking step, NWs disintegrated into smaller crystals with a subsequent decrease in transverse relaxivity (data not shown). The mechanism of disintegration could be the base-catalyzed deprotonation of dextran alcohols and desorption from iron oxide crystals, but it was not investigated further in the present study.

High-resolution transmission electron microscopy images (Figure 2A) of the selected formulations confirmed our previously observed[32] worm-like structure of the nanoparticles, although some nanoclusters were also observed. The particles consisted of multiple crystalline cores aligned in worm-like structures. Magnetization measurements with SQUID confirmed that all particles exhibited classic superparamagnetic behavior. According to Figure 2B, nanoparticles showed no hysteresis at room temperature, and the room-temperature magnetization curves are fit well to a Langevin function. Particles exhibit a Curie-like susceptibility until the blocking temperature is reached and the fluctuations freeze out. Below the blocking temperature there is hysteresis. This is seen in the zero-field-cooled−field-cooled (ZFC-FC) data (Figure 2B) and is consistent classical behavior of superparamagnetic materials.[36] The observed blocking temperatures and saturation magnetization at 300 K (∼95 Am^2/kg, Figure 2C) are consistent with 6−7 nm magnetite.[37]

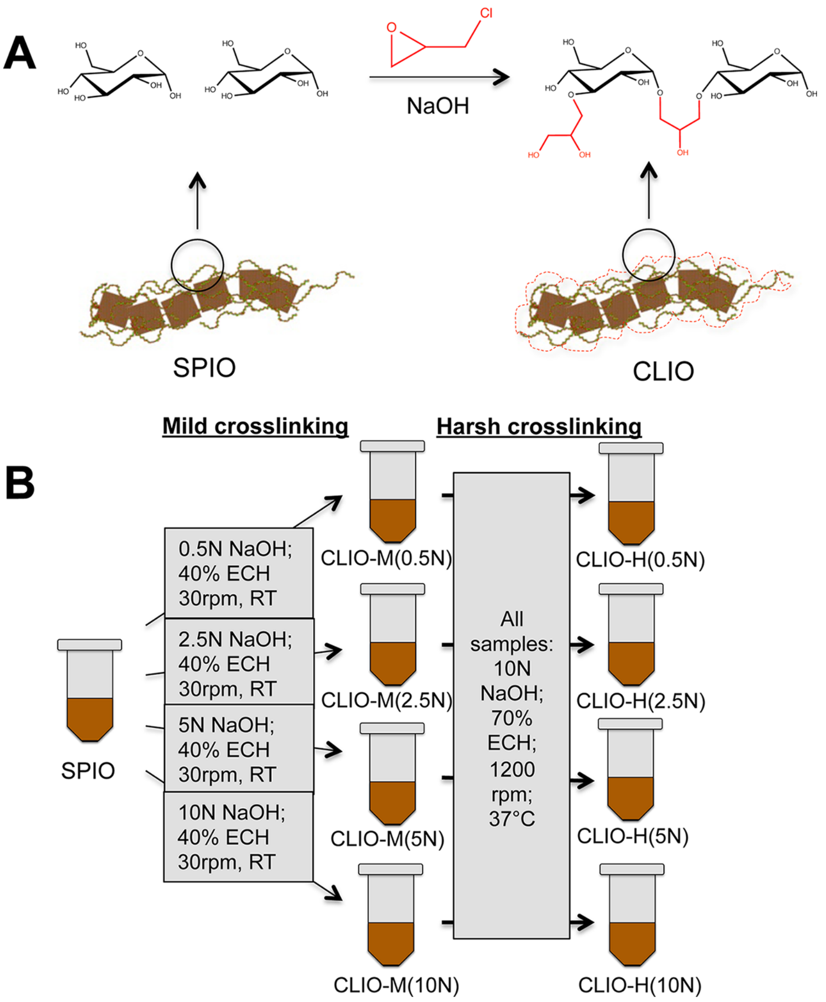

Figure 1. Synthesis of cross-linked nanoworms. (A) Reaction between sugar moieties of dextran and epichlorohydrin (ECH). (B) Two-step synthesis of CLIO from SPIO. The main differences between mild and harsh cross-linking were NaOH and ECH concentrations, temperature, and mixing speed. ECH concentration is v/v; however, it is not miscible with the rest of the components. Note that NaOH normality refers to the stock solution concentration rather than final concentration in the reaction (for details, see Materials and Methods).

The size and relaxivity values of NWs are shown in Table 1. The initial SPIO had around a 250 nm intensity-weighted diameter and molar transverse relaxivity R_2 of 388 mM^{-1} s^{-1}. The cross-linked particles did not show any significant change in the intensity-weighted diameter. The cross-linking did not significantly affect the transverse relaxivity rate R_2 of NWs, except for CLIO-H(10N), which showed decreased relaxivity R_2 of 254 mM^{-1} s^{-1}. However, the R_2 relaxivity values are still much higher than the values previously reported for smaller NWs[13] and commercial iron oxides Feridex and Feraheme (Table 1). The increase in transverse relaxivity values of polycrystalline nanoparticles compared to monocrystalline nanoparticles as a function of aggregate size and number of crystals has been described before,[24] but the exact theoretical reasons for high relaxivity of large nanoworms need to be investigated in the future.

In addition to inter- and intrachain dextran cross-linking, in certain conditions, homopolymerization of ECH occurs,[34] resulting in the formation of a three-dimensional poly(2-hydroxypropyl ether) hydrogel (Figure 3A). We were unable to confirm the polyether formation with Fourier transform infrared spectroscopy (FT-IR) and nuclear magnetic resonance (NMR), due to the overwhelming effect of iron oxide bonds on FTI-IR spectra and the effect of magnetite on relaxation of NMR spectra (not shown). Therefore, we used a modified Baleux iodine assay[38] that has been used for quantitative analysis of polyoxyethylene on the nanoparticle surface,[39] to detect the presence of polyether. Neither dextran nor unmodified SPIO showed any significant iodine reactivity (Supplemental Figure S1). Similarly, mild cross-linking using 0.5–5 N NaOH solution did not produce a detectable iodine reactivity (Figure 3B, Supplemental Figure S1). However, CLIO-M(10N) and all CLIO-H formulations showed a gradual increase in iodine reactivity, with CLIO-H(5N) and CLIO-H(10N) showing the highest iodine reactivity. This experiment confirms formation of polyether structures following cross-linking.

Effects of Cross-Linking on Immunological Properties of Iron Oxide Nanoworms. In order to characterize the effect of

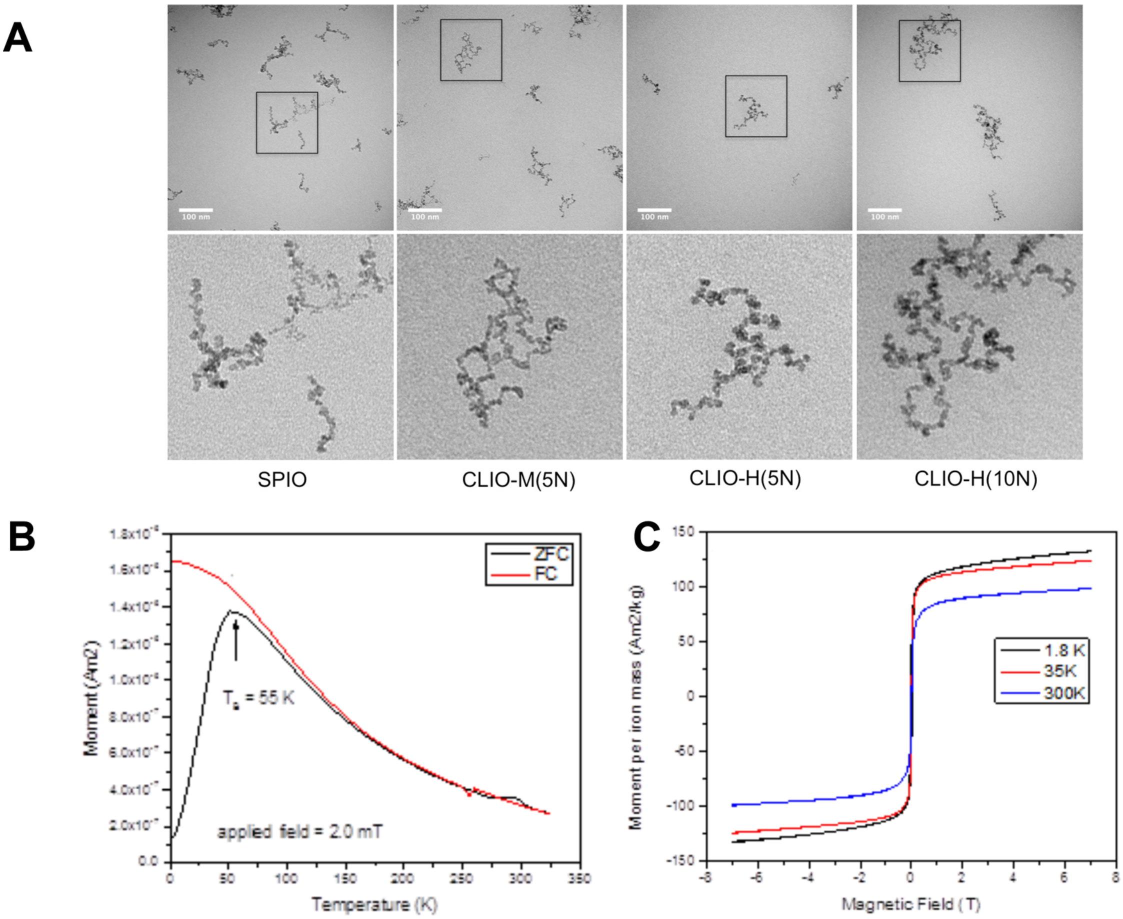

Figure 2. Transmission electron microscopy images and magnetization curves of selected nanoworm formulations. (A) TEM images. Upper panel, low magnification images; lower panel, cropped areas. Images clearly show worm-like particles with electron-dense iron oxide crystals along the strings. The scale bar is 100 nm for the images in the upper panel. (B) SQUID measurements of magnetic moment *vs* temperature (field-cooled and zero-field-cooled–field-cooled curves). Superparamagnetic nanoparticles show a typical hysteresis below Curie blocking temperature. (C) SQUID measurements of magnetic moment *vs* field strength. Saturation magnetization of 95 Am^2/kg is typical for magnetite (see Results). The images and magnetization curves are representative for all formulations tested.

TABLE 1. Measurements of Size and Relaxivity of Nanoworms before and after Cross-Linking

sample name	intensity-weighted hydrodynamic diameter (peak, nm)	R_2 (mM^{-1} s^{-1})
SPIO	253	388
CLIO-M(0.5N)	202	455
CLIO-M(2.5N)	195	365
CLIO-M(5N)	198	320
CLIO-M(10N)	193	308
CLIO-H(0.5N)	277	339
CLIO-H(2.5N)	181	312
CLIO-H(5N)	291	331
CLIO-H(10N)	244	254
Feridex[a]	110	100
Feraheme[a]	35	70

[a] Our measurements.

cross-linking and hydrogel formation on the immune recognition of the NWs, we first measured the binding of anti-dextran antibodies. Since anti-dextran antibodies appear in a significant number of individuals in a general population,[40] the binding of the anti-dextran immunoglobulin G (IgG) is an important, clinically relevant criterion for immunoreactivity of nanoparticles. According to the dot-blot immunoassay, there was no obvious decrease in the binding of anti-dextran IgG to NWs cross-linked in mild conditions at 0.5–5 N NaOH, but there was a significant decrease ($p < 0.0001$) in the binding to NWs cross-linked in mild conditions at 10 N NaOH and to all NWs cross-linked in harsh conditions (Figure 4A). Thus, all CLIO-H showed between 94% and 98% decrease of recognition of anti-dextran IgG (Figure 4A). Next, we used conconavalin A (ConA) as a surrogate probe of sugar reactivity. ConA is a glucose-binding lectin obtained from the jack bean plant *Canavalia ensiformis*. At physiological pH, ConA exists as a 104 kDa tetramer, and each monomer has a glucose-binding site.[41,42] The binding experiments with ConA (Figure 4B) mirrored the results with anti-dextran IgG; that is, there was a significant ($p < 0.0001$), 90%, decrease in ConA binding to CLIO-M(10N) and all CLIO-H formulations.

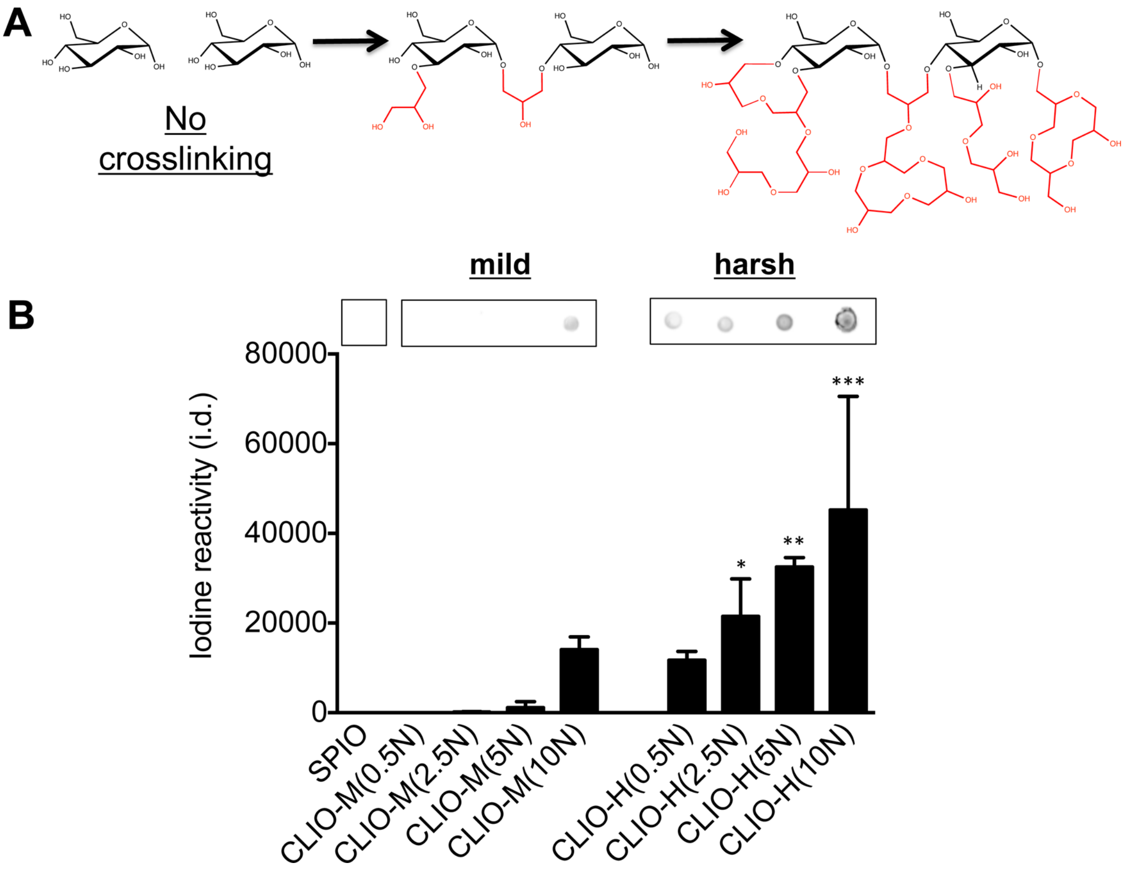

Figure 3. Harsh cross-linking leads to formation of cross-linked polyether on the nanoworm surface. (A) In addition to cross-linking and alkylation of polysaccharide alcohols, epichlorohydrin self-polymerization will lead to formation of poly(2-hydroxypropyl ether). (B) Iodine assay confirmed the formation of polyether on the NW surface in harsh cross-linking conditions. The *y*-axis shows average "integrated density" of each spot in triplicates. Differences between SPIO and CLIO NWs are shown as $^{*}p < 0.05$; $^{**}p < 0.01$; $^{***}p < 0.001$. For statistical analysis, see Materials and Methods.

Nanosurface-grafted polyethylene or poly(propylene oxide)s are known to create a brush border that sterically prevents access of plasma proteins.[43−45] A cross-linked dextran hydrogel on the nanoworm surface could repel dextran-binding proteins *via* a similar mechanism. Therefore, we investigated whether blockade of anti-dextran IgG and ConA binding was due to a specific loss of native sugar epitopes or due to a nonspecific sterical effect. We tested the binding of plasma protein kininogen (120−130 kDa) and its histidine-rich domain 5 kininostatin (fused to glutathione-S-transferase, 33 kDa) that had been previously shown to bind to the iron oxide crystalline core on SPIO and CLIO and not to the nanoworm coating.[32,46] There was a 50% decrease in the binding of D5 and 70% decrease in the binding of kininogen (Figure 4C and D, respectively) to CLIO-H(10N). However, the blockade of absorption of these proteins was much less efficient than that of 104 kDa ConA and 150 kDa anti-dextran IgG. There was no correlation (Spearman coefficient 0.0) between the kininogen and ConA binding (Figure 4E), despite having similar molecular weight. On the other hand, there was a significant correlation (Spearman coefficient 0.7381, $p < 0.05$) between ConA and anti-dextran IgG binding (Figure 4F), suggesting that the cross-linking and hydrogelation block dextran-binding proteins mostly by masking dextran epitopes (Figure 4G), although some steric exclusion effect is also present.

Another important criterion of nanoparticle immunogenicity is complement activation.[47,48] The complement system is responsible for recognition, elimination, and destruction of pathogens.[49] The binding and activation of a complement leads to the assembly of complement component 3 (C3) convertase and covalent deposition of C3b on the pathogen surface, with subsequent uptake *via* complement receptors (*e.g.*, CR3, CR4) on macrophages, monocytes, and neutrophils.[50,51] Moreover, complement cleavage byproducts C3a and C5a are highly potent proinflammatory molecules and macrophage activators with low nanomolar affinity.[52] We questioned whether the surface hydrogelation and loss of dextran immunoreactivity lead to a decrease in the opsonization of the NWs with C3 products. According to dot blot assay (Figure 5A), there was a significant decrease ($p < 0.0001$) in the levels of C3 on CLIO-M(10N) and all CLIO-H formulations. Thus, CLIO-M(10N) showed a 64% decrease in the C3 deposition, whereas CLIO-H(10N) showed over a 90% decrease in the C3

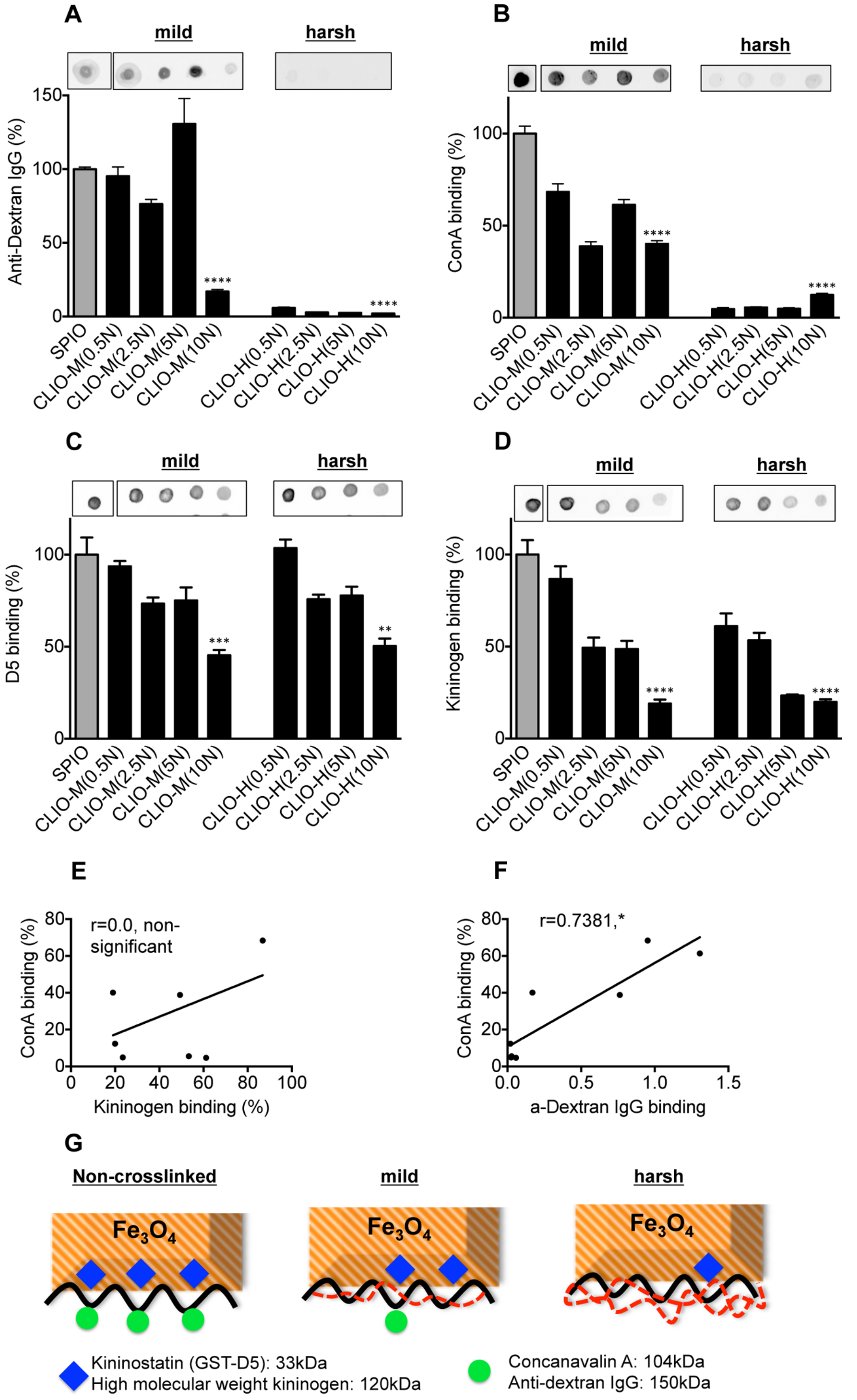

Figure 4. Blockade of dextran immune recognition after cross-linking. Nanoworms were reacted with dextran-specific proteins, anti-dextran antibody (A) and concanavalin A (B), and with iron oxide binding proteins, domain 5 of kininogen (C) and full-length human kininogen (D). The bound proteins were detected with dot blot immunoassay (shown above each of the quantitative densitometry graphs). (E) No correlation between kininogen and ConA binding despite similar sizes of these proteins, suggesting that cross-linking is more selective toward dextran-binding proteins than toward iron oxide-binding proteins. (F) Significant correlation ($p < 0.05$) between anti-dextran antibody binding and ConA binding. Spearman correlation coefficient is shown for all correlation graphs. (G) The graph shows that cross-linked hydrogel blocks dextran immune recognition but is less efficient at blocking iron oxide recognition, suggesting specific blockade of dextran epitopes. Differences between SPIO and CLIO NWs are shown as *$p < 0.05$; **$p < 0.01$; ***$p < 0.001$; ****$p < 0.0001$. For statistical analysis, see Materials and Methods.

deposition. Activation of the complement on the foreign surface occurs *via* either the classical pathway, the lectin (sugar recognition) pathway, or the alternative pathway. In mice, the lectin pathway is triggered

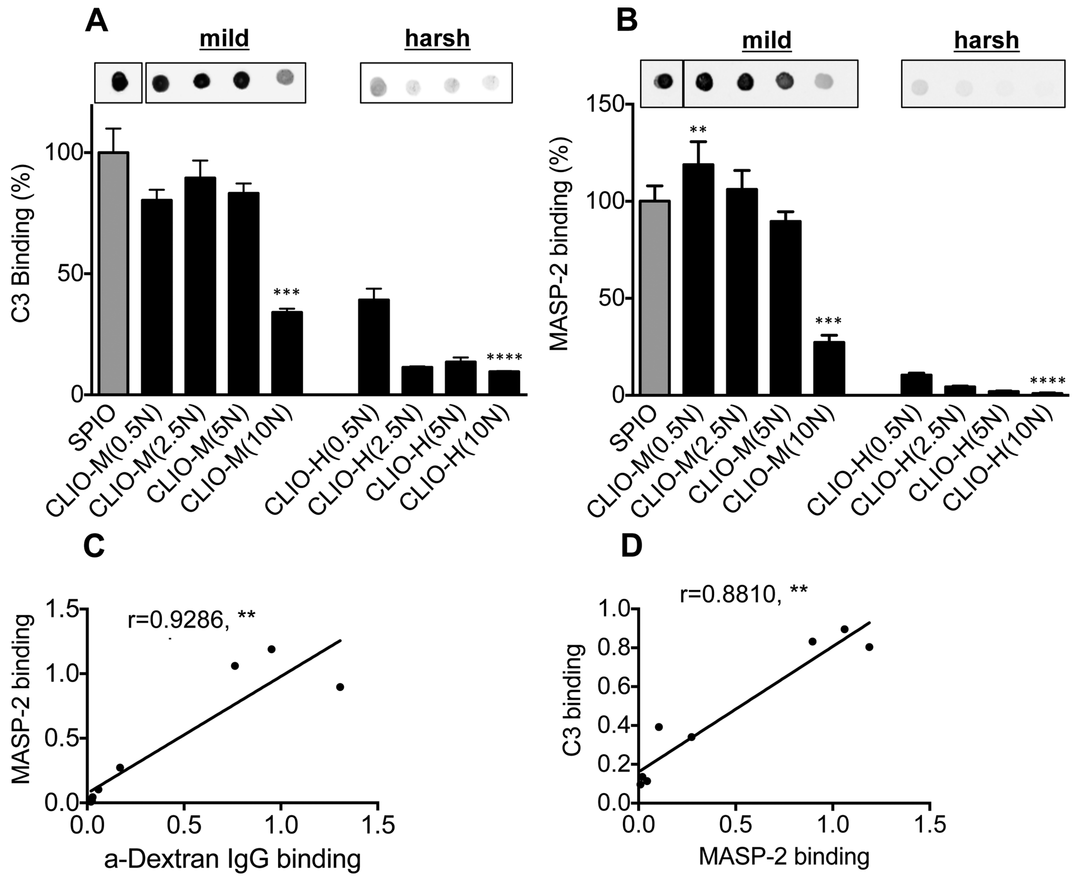

Figure 5. Blockade of mouse complement activation after cross-linking. Nanoworms were incubated in mouse sera, and the binding of C3 and MASP-2 (the lectin pathway serine protease) was detected with immunoblotting. (A) Binding of C3 (C3b); (B) binding of MASP-2; (C) significant correlation (p < 0.01) between dextran immunoreactivity and MASP-2 binding; (D) significant correlation (p < 0.01) between MASP-2 binding and C3 opsonization. The results suggest that cross-linking mostly blocks the sugar recognition pathway (lectin pathway) of mouse complement. Spearman correlation coefficient is shown for all correlation graphs. Differences between SPIO and CLIO NWs are shown as **p < 0.01; ***p < 0.001; ****p < 0.0001. For statistical analysis, see Materials and Methods.

through initial binding of mannose-binding lectin (MBL-A/C) and MBL-associated serum protease MASP-2, leading to formation of classical C3 convertase.[49] According to Figure 5B, there was over a 90% decrease in the binding of MASP-2 to all CLIO-H NWs. There was a significant correlation between dextran immunoreactivity and MASP-2 binding (Figure 5C, Spearman coefficient 0.9286, p < 0.05) and a significant correlation between MASP-2 binding and C3 opsonization (Figure 5D, Spearman coefficient 0.8810, p < 0.05). On the basis of these data, we suggest that cross-linking prevents complement activation by blocking the lectin pathway in mouse sera, which needs to be investigated further. At the same time, it must be noted that because mouse and human complement systems are similar but not identical,[53] the effect of cross-linking on human complement activation cannot be extrapolated from mouse serum data and will be the subject of a separate study.

Effects of Cross-Linking on Nanoworm Uptake by Macrophages. In order to determine the effect of cross-linking on the uptake by macrophages *in vitro*, we incubated NWs with freshly isolated peritoneal macrophages (PMF) with or without mouse sera. Nanoworms were incubated with mouse sera (1:3 v/v) for 15 min prior to addition to macrophages. According to the images of Prussian blue staining (Figure 6A), there was a high level of uptake of Fe in SPIO- and CLIO-M(5N)-treated PMF, whereas CLIO-M(5N)- and CLIO-H(10N)-treated PMF showed much less uptake of Fe. Quantification of Fe uptake (Figure 6B) showed an interesting trend: SPIO was taken up either with or without serum, but the uptake was significantly (p < 0.0001) higher in serum. CLIO-M(0.5−5N) uptake was also significantly (p < 0.0001) dependent on serum, whereas CLIO-M(10N) and all CLIO-H showed minimal uptake either with or without serum (98% decrease compared to SPIO, p < 0.0001). The mechanisms of serum-independent uptake are not clear. Previously we demonstrated that macrophage scavenger receptors are capable of recognizing SPIO[54] *via* a negatively charged iron oxide core and that surface coating sterically blocks recognition of negatively charged iron oxide by the collagen-like domain of scavenger receptor SR-AI/II.[55] It is possible that SPIO is recognized in serum *via* both scavenger-receptor-dependent and complement-dependent

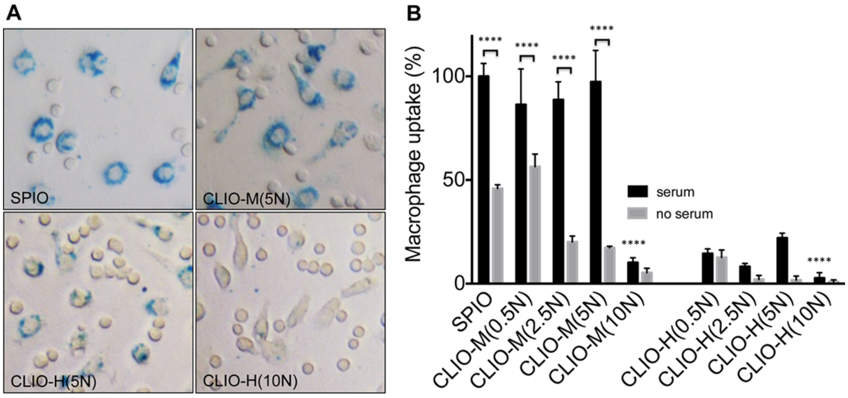

Figure 6. Uptake of nanoworms by peritoneal macrophages. (A) Prussian blue staining of macrophages after 3 h incubation with 0.1 mg/mL nanoworms in mouse serum. (B) Iron uptake quantification with or without serum. Notably, SPIO and mild cross-linked CLIO show significant serum-dependent and -independent uptake, whereas CLIO-M(10N) and CLIO-H show minimal serum-dependent and -independent uptake. Differences between SPIO and CLIO NWs and within the same NW group between serum and no serum conditions are shown as ****$p < 0.0001$. For statistical analysis, see Materials and Methods.

mechanisms and that the effect of cross-linking on NW uptake by macrophages is due to the blockade of both mechanisms of uptake, but this hypothesis needs to be studied further.

Effect of Cross-Linking on Clearance and Toxicity of Iron Oxide Nanoworms *in Vivo*. One of the most serious problems of nanomedicines is the avid recognition and clearance by liver and spleen macrophages.[45,56] Premature clearance shortens nanoparticle half-life in circulation and drastically decreases the bioavailability of nanoparticles. This is especially the issue with larger nanoparticles.[44,57] We measured circulation half-life of SPIO and selected CLIO formulations following intravenous injection in mice. SPIO had a plasma half-life of 8 ± 2 min, CLIO-M(5N), 67 ± 26 min, and CLIO-H(5N), 198 ± 114 min. CLIO-H(10N) showed a highly significant ($p < 0.001$) increase in half-life to 574 ± 203 min (Figure 7A,B). To understand whether the short circulation half-life of SPIO is due to the desorption of dextran chains in serum, we incubated SPIO in mouse serum for 15 min, washed with an ultracentrifuge, and probed the NWs with anti-dextran IgG. There was no loss of dextran coating after incubation of SPIO in serum (Supplemental Figure S2). As previously reported,[32] SPIO exhibited a strong accumulation in Kupffer cells in the liver (not shown here). CLIO-M(5N) exhibited significant Kupffer cell accumulation (Figure 7C), whereas CLIO-H(10N) showed no visible uptake by Kupffer cells (20 h postinjection). According to Prussian blue staining (Figure 7C), both CLIO-M(5N) and CLIO-H(10N) accumulated in the spleen, while the kidneys did not accumulate nanoparticles. Nanoparticles mostly colocalized with the F4/80-positive marginal zone macrophages in the spleen (Supplemental Figure S3), suggesting that the spleen eventually clears nanoparticles that evade the liver uptake. To determine whether the size of CLIO-H(10N) with a long circulation half-life changed *in vivo*, we used a magnetic column to recover CLIO-H(10N) NWs from blood 6 h postinjection. According to size measurements (Figure 7D), NWs recovered from mice had the same size (250 nm, intensity weighted diameter) as before the injection, and the size agreed with TEM images of NWs recovered from blood (Figure 7E). The long-circulating properties of 250 nm CLIO-H(10N) and lack of recognition by Kupffer cells are surprising findings, in view of the fact that large size is known to promote nanoparticle clearance,[44,57] and we are not aware of other examples of iron oxide nanoparticles of this size range having a 10 h half-life in mice. Interestingly, there was a 2.8-fold difference between CLIO-H(5N) and CLIO-H(10N). CLIO-H(5N) and CLIO-H(10N) are similar in terms of size and immune recognition, but CLIO-H(10N) showed slightly higher (albeit not statistically significant) iodine reactivity, suggesting more polyether coating. Although we cannot say at this point which macrophage receptors and mechanisms are responsible for the clearance of NWs, it is plausible to suggest that formation of a hydrogel coating together with prevention of the complement C3 opsonization and alteration of dextran structure could all be responsible for the increase in the circulation half-life following harsh cross-linking, but further investigation of the mechanisms of immunological recognition of the NWs is definitely needed. Lastly, in order to test the toxicity of nanoworms, mice were injected with SPIO, CLIO-M(5N), and CLIO-H(10N) and weighed daily for 7 days. There was no decrease in mouse weight in all experimental groups (Supplemental Figure S4). Serum aspartate aminotransferase (AST), which is the enzyme that becomes elevated in liver damage, was normal in all the experimental groups and did not differ significantly from the control mice (Table 2). Further, we collected the organs of injected and noninjected mice and stained the histological sections of liver, spleen, kidneys, lungs, and brain with hematoxylin–eosin. According to

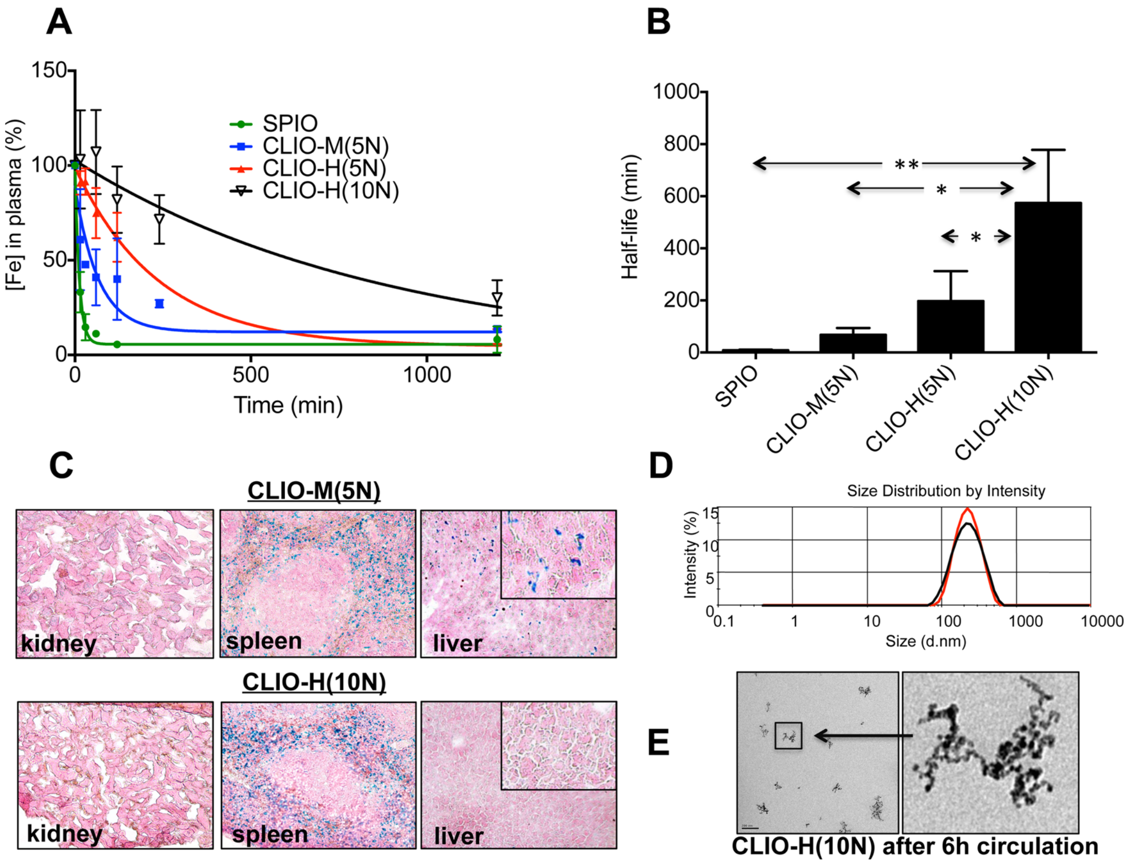

Figure 7. *In vivo* clearance and Kupffer cell uptake after cross-linking. (A) Nanoworms were injected into mice ($n = 3$ or 4 per group), and the levels of iron in plasma were measured. The curve was fitted to a monoexponential decay. (B) Average (±standard deviation) half-life in plasma shows the long-circulating properties of harsh-cross-linked CLIO. Differences between SPIO and CLIO NWs are shown as $*p < 0.05$; $**p < 0.01$. (C) Histological sections of kidney, spleen, and liver 20 h postinjection show lack of uptake of CLIO-H(10N) particles by the Kupffer cells in the liver and the uptake by the marginal zone macrophages in the spleen (see Supplemental figure S3). (D) CLIO-H(10N) particles were recovered from blood samples 6 h postinjection. Size data show CLIO-H(10N) intensity weighted diameter before (black trace) and after (red trace) injection (E) TEM image of CLIO-H(10N) recovered from blood 6 h postinjection. The scale bar on the low-magnification image (left) is 100 nm.

TABLE 2. Measured Levels (IU/L) of Aspartate Transaminase (AST) Following Intravenous Injection into Male BALB/c Mice[a]

	control		day 1		day 4		day 6		day 7	
group	mean	SD	mean	SD	mean	SD	mean	SD	mean	SD
SPIO	46.0	12.5	102.9	92.7	70.0	36.7	84.4	53.7	61.1	3.3
CLIO-M(5N)	94.9	95.3	77.8	51.2	179.9	174.4	37.4	16.8	35.5	9.8
CLIO-H(10N)	38.4	13.9	46.8	23.5	59.5	49.3	65.6	38.7	38.1	24.4

[a] AST levels (indicator of liver damage) are within a normal range of values (up to 255 IU/L in male mice, retro-orbital collection[64]). $N = 3$ for all groups. SD = standard deviation.

Supplemental Figure S5, no signs of tissue necrosis, inflammation, or thrombosis were observed histologically.

CONCLUSION

In this work we set out to study the effect of base-catalyzed cross-linking of the dextran shell of large, high-relaxivity SPIO NWs with 1-chloro-2,3-epoxypropane on the size, relaxivity, and immune recognition.

The important finding was that increasing the concentration of NaOH, agitation speed, and temperature caused a progressive loss in the immunoreactivity of dextran on the NWs, as evidenced by loss of binding of anti-dextran IgG and ConA. Moreover, with the increase in NaOH concentration and dextran modification, there was a loss of binding of critical lectin pathway protease MASP-2 and over 90% decrease in the C3 opsonization in mouse serum. The reduction of NW immune recognition translated unexpectedly into a long *in vivo* half-life of 250 nm NWs, suggesting that ECH cross-linking could offer a straightforward strategy to reduce the immunoreactivity of large carbohydrate-coated iron oxides. Importantly, the bioinertness could be achieved *via* surface hydrogelation rather than PEGylation. Since PEG chains are known to prevent interaction of targeted nanoparticles with the target receptors,[58,59] it would be interesting to compare the targeting properties of our CLIO and PEGylated iron oxides. Our work suggests that long-circulating MRI contrast agents with high R_2 relaxivity can be manufactured in a simple, scalable procedure using commonly available pharmaceutical excipients. There is a balance between the harshness of cross-linking needed to achieve long-circulating properties and its decreasing effects on relaxivity. Due to high relaxivity, long-circulating properties, and low complement activation, we envision important applications of these nanoparticles, including molecular MRI of tumors for improving specificity of imaging of the cancer process[60−62] or magnetic labeling for *in vivo* cell tracking.[26,63]

MATERIALS AND METHODS

Materials. All chemical reagents used for nanoworm synthesis including iron salts and 15−25 kDa dextran were purchased from Sigma-Aldrich (St. Louis, MO, USA). Cell culture media were purchased from Corning Life Sciences. Anti-dextran DX-1 antibody was purchased from StemCell Technologies (Vancouver, BC, Canada). Goat anti-mouse anti-complement C3 antibody was purchased from MP Biomedicals (Solon, OH, USA). Goat anti-human domain 5 and mouse anti-human kininogen antibodies were from R&D Systems. Goat anti-human/mouse MASP-2 antibody was from Santa Cruz Biotechnology Inc. (Santa Cruz, CA, USA). Human high molecular weight kininogen was purchased from R&D Systems. For production of recombinant domain 5 (D5) of human kininogen, the fusion GST-D5 was cloned into pGEX vector and expressed in a BL21 system. GST-D5 fusion was purified in a glutathione-sepharose affinity column, eluted by a 5 mM reduced glutathione buffer. and dialyzed against phosphate-buffered saline (PBS) before use. Concanavalin A (fluorescein labeled) was purchased from Life Technologies (Carlsbad, CA, USA). Copper grids (300 mesh) were purchased from Electron Microscopy Sciences (Hatfield, PA, USA). BALB/c mice were bred in an animal vivarium at the University of Colorado Denver Anschutz Medical Campus according to the IACUC approved breeding protocol. The BALB/c breeder mice were purchased from Charles River Laboratories International, Inc. (Wilmington, MA, USA).

Synthesis of Superparamagnetic Iron Oxide and Cross-Linked Iron Oxide Nanoworms. Nanoworms were synthesized using a one-pot Molday and MacKenzie[2] precipitation method. Nanopure water was deoxygenated with nitrogen gas and used to dissolve 3 g of dextran (molecular weight 20 K, Sigma-Aldrich), 0.42 g of Fe(III) chloride, and 0.166 g of Fe(II) chloride in a round-bottom flask. Then, 0.75 mL of a cold 25% solution of ammonium hydroxide (Acros Organics) was slowly added to the mixture of dextran and iron salts under a nitrogen atmosphere with rapid stirring on ice. After formation of NWs, the mixture was oil-bathed at 80 °C in the open air with stirring. After cooling, SPIO was purified overnight using a 1 MDa dialysis bag (Spectrum Chemicals, New Brunswick, NJ, USA) against water to remove extra free dextran. The SPIO was chemically cross-linked using 1-chloro-2,3-epoxypropane (epichlorohydrin or ECH) with sodium hydroxide as a catalyst. The cross-linked iron oxide NWs were prepared in two steps: first, in a mild step by mixing 40% SPIO solution (1−2 mg/mL), 20% NaOH (0.5, 2.5, 5, and 10 N), and 40% ECH. The mixture was gently rotated at 30 rpm overnight at 23 °C to form CLIO-Mild (CLIO-M) NWs. Second, the harsh step consisted of mixing 20% CLIO-M, 10% NaOH (10N), and 70% ECH and shaking at 1200 rpm overnight at 37 °C to form CLIO-Harsh (CLIO-H) NWs. CLIOs were centrifuged to remove the layer of ECH and then dialyzed to remove the remaining NaOH and ECH. The SPIO and CLIO were filtered through a 0.45 μm pore filter (Millipore, Billerica, MA, USA) prior to use.

Magnetization Measurements. Fe concentrations of NWs were determined by measuring the absorbance at a wavelength of 400 nm using a Spectromax M5 microplate reader (Molecular Devices, Sunnyvale, CA, USA). The magnetic measurements were made on a commercial superconducting quantum interference device (SQUID) magnetometer (Quantum Design MPMS). Samples were prepared by pipetting 100 mL of fluid with Fe concentrations of approximate 1.2 mg/mL into small, thin-wall polypropylene vials, which were subsequently heat sealed. The samples were cooled in zero field, and then the moment was measured upon warming in a 2 mT field. Subsequently, the moment was measured as the sample was cooled to obtain the field-cooled data. The moment *versus* magnetic field curves were subsequently measured at 1.8, 35, and 300 K. An additional magnetization curve was than measured by cooling back down to 1.8 K to determine if any changes occurred in the magnetic particle configuration on exposure to high fields and varying temperatures. After field cycling and freezing and thawing cycles, moments at 1.8 K, 7 T were observed to decrease by 6% to 20% depending on the sample. The measured moment was corrected by subtracting out the diamagnetic signals from the water and the polypropylene sample holder. The diamagnetic correction was determined from the measured masses of the sample, which is mostly water, the sample container, and the measured values for the diamagnetic susceptibility of water and polypropylene. The moment was then converted to mass magnetization by dividing the moment by the measured Fe concentration and the sample volume (100 mL).

Size and Shape Measurements. Transmission electron microscopy (TEM) imaging was conducted to visualize the NWs using a FEI Tecnai Spirit BioTwin electron microscope (Electron Microscopy Facility at the University of Colorado Boulder) at a 100 kV working voltage. Size and zeta potential measurements of NPs were determined using a Zetasizer Nano ZS (Malvern Instruments Ltd., Malvern, UK). The intensity-weighted size distribution peak value was used to report hydrodynamic diameters of NWs.

Transverse Relaxivity Measurements. Transverse relaxivity measurements of NWs were performed with a 4.7 T Bruker PharmaScan MRI with a 64 mm birdcage receiver/transmitter RF coil using MSME (multislice multiecho) T_2-weighted pulse sequences. Briefly, two axial slices were placed with a field of view of 4 mm, a slice thickness of 1.5 mm, and 1.8 mm slice distance. T_2 weighting and calculation was achieved by using repetition times (TR) of 2650 ms and 16 echo times (TE = 10, 20, 30, 40, *etc.*, ms). The matrix size of 128 × 256 resulted in a total scan time of 11 min. The inverted T_2 values ($1/T_2$) were plotted *versus* Fe concentrations, and the molar relaxivity rates were determined as the slope of the linear curve. For iodine reactivity, 2 μL NW solutions at 0.5 mg/mL concentrations were applied in triplicate on a nitrocellulose membrane (0.45 μm, Bio-Rad Laboratories, Inc., Hercules, CA, USA) and allowed to dry briefly, and 5 μL of 5% Lugol's iodine solution was applied onto each spot. Membranes were dried under laminar flow in a biosafety cabinet, and the reverse side of the membrane was scanned with a flatbed scanner. The images were converted into 8-bit; the background was subtracted and the integrated intensity of the spots was determined using ImageJ software and plotted with Prism software.

Dot Blot Protein Binding Assay. For binding of anti-dextran antibody, SPIO and CLIO NWs (2 μL of 0.2 mg/mL) were applied in triplicate onto a nitrocellulose membrane. For binding of complement C3 and MASP-2 in mouse serum, SPIO and CLIO NWs (50 μL of 0.2 mg/mL) were incubated with 20 μL of mouse serum for 15 min at RT. At the end of incubation, particles were washed three times with 1× PBS by centrifugation at 55 000 rpm at RT using a Beckman Optima TLX ultracentrifuge. The pellets were resuspended in 20 μL of PBS, and 2 μL aliquots were applied in triplicate onto a nitrocellulose membrane. For binding of recombinant D5, human kininogen, and ConA proteins, NWs (50 μL of 0.2 mg/mL in PBS) were incubated with either 1 μL of 1 mg/mL ConA, 10 μL of 0.35 mg/mL D5, or 10 μL of 1 mg/mL kininogen for 15 min at RT. Nanoworms were washed three times with 1× PBS by centrifugation at

55 000 rpm at RT. The pellets were then resuspended in 20 μL of PBS, and 2 μL aliquots were applied in triplicate onto a nitrocellulose membrane. The membranes were blocked using 5% nonfat dry milk in PBS-T (1× PBS with 0.1% Tween 20) for 1 h at RT and probed with corresponding primary antibodies for 1 h at RT, followed by washing the membranes three times with PBS-T and finally 1 h incubation with the corresponding IRDye 800CW-labeled secondary antibodies against the primary antibody species (see Materials and Methods). The membranes after immunoblotting were visualized using an Odyssey infrared imager (Li-COR Biosciences, Lincoln, NE, USA). The integrated dot intensity in the scanned images was quantitatively analyzed using ImageJ software and Prism 6 software (GraphPad Software, Inc., La Jolla, CA, USA).

Macrophage Uptake of SPIO and CLIO Nanoworms. Mouse peritoneal macrophages were obtained by peritoneal lavage with 5 mL of cold PBS, post-mortem. The macrophages were washed once with RPMI 1640, resuspended in RPMI 1640 at approximately 1 million cells/mL, and plated at 50 μL per well in a 96-well plate for 2 h. The NWs were added to macrophages at 0.1 mg/mL Fe concentration in the presence or absence of mouse serum and incubated for 3 h. After the incubation, macrophages were washed three times with PBS, fixed in 4% paraformaldehyde for 1 h, and then stained by Prussian blue for 30 min. Cell imaging was conducted using a Nikon Eclipse microscope under transmitted light. The Fe concentration in macrophages was determined using a ferrazine QuantiChrome iron assay kit as described.[6]

***In Vivo* Pharmacokinetics of SPIO and CLIO Nanoworms.** All experiments were performed under the University of Colorado-approved IACUC protocol 103914(02)1E. NWs (0.25 mg/mL, 200 μL in PBS) were injected into mice (4−6 week old, female BALB/c) *via* tail vein. Blood collections were conducted with heparinated capillaries using the retro-orbital method at 1 min and several time points thereafter, up to 20 h postinjection. The experiments were conducted with 3 or 4 mice per group. The collected blood samples were centrifuged at maximum speed for 5 min using a tabletop microfuge. The relative Fe concentrations in plasma were determined using a QuantiChrome iron assay kit (using 1 min time point as 100% value). The percentages of particles in plasma *versus* time points were plotted using Prism 6 software and fitted into monoexponential decay to derive circulation half-life. The liver and spleen organs were collected, frozen in liquid nitrogen, and embedded in optical coherence tomography (OCT) liquid for histological sections. Frozen OCT-embedded tissues were sectioned using a Leica CM1850 cryostat (Leica Biosystems) and air-dried. The sections were then fixed using formalin (10%, diluted from 37% stock formalin solution) for 1 h and stained with Prussian blue solution (made in house) for 30 min and counterstained with Nuclear Fast Red solution (Sigma-Aldrich) for 15 min. Imaging of sections was done using a Nikon light microscope.

Statistical Analysis. All statistical analysis was performed using Prism 6 software. Differences in protein binding between SPIO as the control group and each NW group were analyzed with multiple t tests assuming 95% confidence interval. Differences in macrophage uptake were analyzed by two-way ANOVA with multiple comparisons. Differences in half-life between animal groups were analyzed with a two-tailed parametric t test using Prism 6 software assuming a 95% confidence interval. Differences of $p < 0.05$ were considered to be statistically significant. The correlation coefficients between protein bindings and macrophage uptake were computed using Prism 6 software assuming a nonparametric Spearman correlation with two-tailed p-value, 95% confidence interval. Differences in all data are shown as $*p < 0.05$; $**p < 0.01$; $***p < 0.001$; $****p < 0.0001$.

Conflict of Interest: The authors declare no competing financial interest.

Acknowledgment. This study was funded by the University of Colorado Denver startup funds to D.S. We would like to thank Drs. Thomas Anchordoquy and S. Moien Moghimi for useful discussions and Mr. James J. Hesson for editing the manuscript.

Supporting Information Available: This material is available free of charge *via* the Internet at http://pubs.acs.org.

REFERENCES AND NOTES

1. Gupta, A. K.; Gupta, M. Synthesis and Surface Engineering of Iron Oxide Nanoparticles for Biomedical Applications. *Biomaterials* **2005**, *26*, 3995–4021.
2. Molday, R. S.; MacKenzie, D. Immunospecific Ferromagnetic Iron-Dextran Reagents for the Labeling and Magnetic Separation of Cells. *J. Immunol. Methods* **1982**, *52*, 353–367.
3. Boehm, H. Acidic and Basic Properties of Hydroxylated Metal Oxide Surfaces. *Discuss. Faraday Soc.* **1971**, *52*, 264–275.
4. Jung, C. W. Surface Properties of Superparamagnetic Iron Oxide MR Contrast Agents: Ferumoxides, Ferumoxtran, Ferumoxsil. *Magn. Reson. Imaging* **1995**, *13*, 675–691.
5. Raynal, I.; Prigent, P.; Peyramaure, S.; Najid, A.; Rebuzzi, C.; Corot, C. Macrophage Endocytosis of Superparamagnetic Iron Oxide Nanoparticles: Mechanisms and Comparison of Ferumoxides and Ferumoxtran-10. *Invest. Radiol.* **2004**, *39*, 56–63.
6. Simberg, D.; Park, J. H.; Karmali, P. P.; Zhang, W. M.; Merkulov, S.; McCrae, K.; Bhatia, S. N.; Sailor, M.; Ruoslahti, E. Differential Proteomics Analysis of the Surface Heterogeneity of Dextran Iron Oxide Nanoparticles and the Implications for Their in Vivo Clearance. *Biomaterials* **2009**, *30*, 3926–3933.
7. Bulte, J. W.; Kraitchman, D. L. Iron Oxide MR Contrast Agents for Molecular and Cellular Imaging. *NMR Biomed.* **2004**, *17*, 484–5499.
8. Moore, A.; Weissleder, R.; Bogdanov, A., Jr. Uptake of Dextran-Coated Monocrystalline Iron Oxides in Tumor Cells and Macrophages. *J. Magn. Reson. Imaging: JMRI* **1997**, *7*, 1140–1145.
9. Kiessling, F.; Mertens, M. E.; Grimm, J.; Lammers, T. Nanoparticles for Imaging: Top or Flop? *Radiology* **2014**, *273*, 10–28.
10. Nahrendorf, M.; Keliher, E.; Marinelli, B.; Waterman, P.; Feruglio, P. F.; Fexon, L.; Pivovarov, M.; Swirski, F. K.; Pittet, M. J.; Vinegoni, C.; Weissleder, R. Hybrid PET-Optical Imaging Using Targeted Probes. *Proc. Natl. Acad. Sci. U.S.A.* **2010**, *107*, 7910–7915.
11. Wunderbaldinger, P.; Josephson, L.; Weissleder, R. Cross-linked Iron Oxides (CLIO): A New Platform for the Development of Targeted MR Contrast Agents. *Acad. Radiol* **2002**, *9* (Suppl 2), S304–306.
12. Park, J. H.; von Maltzahn, G.; Zhang, L.; Derfus, A. M.; Simberg, D.; Harris, T. J.; Ruoslahti, E.; Bhatia, S. N.; Sailor, M. J. Systematic Surface Engineering of Magnetic Nanoworms for in Vivo Tumor Targeting. *Small* **2009**, *5*, 694–700.
13. Park, J. H.; von Maltzahn, G.; Zhang, L.; Schwartz, M. P.; Ruoslahti, E.; Bhatia, S.; Sailor, M. J. Magnetic Iron Oxide Nanoworms for Tumor Targeting and Imaging. *Adv. Mater.* **2008**, *20*, 1630–1635.
14. Agemy, L.; Sugahara, K. N.; Kotamraju, V. R.; Gujraty, K.; Girard, O. M.; Kono, Y.; Mattrey, R. F.; Park, J. H.; Sailor, M. J.; Jimenez, A. I.; Cativiela, C.; Zanuy, D.; Sayago, F. J.; Aleman, C.; Nussinov, R.; Ruoslahti, E. Nanoparticle-Induced Vascular Blockade in Human Prostate Cancer. *Blood* **2010**, *116*, 2847–2856.
15. Park, J. H.; von Maltzahn, G.; Xu, M. J.; Fogal, V.; Kotamraju, V. R.; Ruoslahti, E.; Bhatia, S. N.; Sailor, M. J. Cooperative Nanomaterial System to Sensitize, Target, and Treat Tumors. *Proc. Natl. Acad. Sci. U.S.A.* **2010**, *107*, 981–986.
16. von Maltzahn, G.; Park, J. H.; Lin, K. Y.; Singh, N.; Schwoppe, C.; Mesters, R.; Berdel, W. E.; Ruoslahti, E.; Sailor, M. J.; Bhatia, S. N. Nanoparticles That Communicate in Vivo to Amplify Tumour Targeting. *Nat. Mater.* **2011**, *10*, 545–552.
17. Ren, Y.; Cheung, H. W.; von Maltzhan, G.; Agrawal, A.; Cowley, G. S.; Weir, B. A.; Boehm, J. S.; Tamayo, P.; Karst, A. M.; Liu, J. F.; Hirsch, M. S.; Mesirov, J. P.; Drapkin, R.; Root, D. E.; Lo, J.; Fogal, V.; Ruoslahti, E.; Hahn, W. C.; Bhatia, S. N. Targeted Tumor-Penetrating Sirna Nanocomplexes for Credentialing the Ovarian Cancer Oncogene Id4. *Sci. Transl. Med.* **2012**, *4*, 147ra112.
18. Girard, O. M.; Du, J.; Agemy, L.; Sugahara, K. N.; Kotamraju, V. R.; Ruoslahti, E.; Bydder, G. M.; Mattrey, R. F. Optimization

of Iron Oxide Nanoparticle Detection Using Ultrashort Echo Time Pulse Sequences: Comparison of T1, T2*, and Synergistic T1-T2* Contrast Mechanisms. *Magnetic Reson. Med.* **2011**, *65*, 1649–1660.

19. Thorek, D. L.; Chen, A. K.; Czupryna, J.; Tsourkas, A. Superparamagnetic Iron Oxide Nanoparticle Probes for Molecular Imaging. *Ann. Biomed. Eng.* **2006**, *34*, 23–38.
20. LaConte, L. E.; Nitin, N.; Zurkiya, O.; Caruntu, D.; O'Connor, C. J.; Hu, X.; Bao, G. Coating Thickness of Magnetic Iron Oxide Nanoparticles Affects R2 Relaxivity. *J. Magn. Reson. Imaging: JMRI* **2007**, *26*, 1634–1641.
21. Tong, S.; Hou, S. J.; Zheng, Z. L.; Zhou, J.; Bao, G. Coating Optimization of Superparamagnetic Iron Oxide Nanoparticles for High T-2 Relaxivity. *Nano Lett.* **2010**, *10*, 4607–4613.
22. Choo, E. S. G.; Tang, X. S.; Sheng, Y.; Shuter, B.; Xue, J. M. Controlled Loading of Superparamagnetic Nanoparticles in Fluorescent Nanogels as Effective T-2-Weighted MRI Contrast Agents. *J. Mater. Chem.* **2011**, *21*, 2310–2319.
23. Yoon, T. J.; Lee, H.; Shao, H.; Hilderbrand, S. A.; Weissleder, R. Multicore Assemblies Potentiate Magnetic Properties of Biomagnetic Nanoparticles. *Adv. Mater.* **2011**, *23*, 4793–4797.
24. Poselt, E.; Kloust, H.; Tromsdorf, U.; Janschel, M.; Hahn, C.; Masslo, C.; Weller, H. Relaxivity Optimization of a Pegylated Iron-Oxide-Based Negative Magnetic Resonance Contrast Agent for T(2)-Weighted Spin-Echo Imaging. *ACS Nano* **2012**, *6*, 1619–16124.
25. Gazeau, F.; Levy, M.; Wilhelm, C. Optimizing Magnetic Nanoparticle Design for Nanothermotherapy. *Nanomedicine (London)* **2008**, *3*, 831–844.
26. Wu, Y. J.; Muldoon, L. L.; Varallyay, C.; Markwardt, S.; Jones, R. E.; Neuwelt, E. A. In Vivo Leukocyte Labeling with Intravenous Ferumoxides/Protamine Sulfate Complex and in Vitro Characterization for Cellular Magnetic Resonance Imaging. *Am. J. Physiol.* **2007**, *293*, C1698–1708.
27. Arbab, A. S.; Yocum, G. T.; Kalish, H.; Jordan, E. K.; Anderson, S. A.; Khakoo, A. Y.; Read, E. J.; Frank, J. A. Efficient Magnetic Cell Labeling with Protamine Sulfate Complexed to Ferumoxides for Cellular MRI. *Blood* **2004**, *104*, 1217–1223.
28. Janic, B.; Iskander, A. S.; Rad, A. M.; Soltanian-Zadeh, H.; Arbab, A. S. Effects of Ferumoxides-Protamine Sulfate Labeling on Immunomodulatory Characteristics of Macrophage-Like Thp-1 Cells. *PloS One* **2008**, *3*, e2499.
29. Lanza, G. M.; Caruthers, S. D.; Winter, P. M.; Hughes, M. S.; Schmieder, A. H.; Hu, G.; Wickline, S. A. Angiogenesis Imaging with Vascular-Constrained Particles: The Why and How. *Eur. J. Nucl. Med. Mol. Imaging* **2010**, *37* (Suppl 1), S114–126.
30. Howard, M.; Zern, B. J.; Anselmo, A. C.; Shuvaev, V. V.; Mitragotri, S.; Muzykantov, V. Vascular Targeting of Nanocarriers: Perplexing Aspects of the Seemingly Straightforward Paradigm. *ACS Nano* **2014**, *8*, 4100–4132.
31. Byrne, J. D.; Betancourt, T.; Brannon-Peppas, L. Active Targeting Schemes for Nanoparticle Systems in Cancer Therapeutics. *Adv. Drug Delivery Rev.* **2008**, *60*, 1615–1626.
32. Karmali, P. P.; Chao, Y.; Park, J. H.; Sailor, M. J.; Ruoslahti, E.; Esener, S. C.; Simberg, D. Different Effect of Hydrogelation on Antifouling and Circulation Properties of Dextran-Iron Oxide Nanoparticles. *Mol. Pharmaceutics* **2012**, *9*, 539–545.
33. Denizli, B. K.; Can, H. K.; Rzaev, Z. M. O.; Guner, A. Preparation Conditions and Swelling Equilibria of Dextran Hydrogels Prepared by Some Crosslinking Agents. *Polymer* **2004**, *45*, 6431–6435.
34. Renard, E.; Deratani, A.; Volet, G.; Sebille, B. Preparation and Characterization of Water Soluble High Molecular Weight Beta-Cyclodextrin-Epichlorohydrin Polymers. *Eur. Polym. J.* **1997**, *33*, 49–57.
35. Holmberg, L.; Lindberg, B.; Lindqvist, B. The Reaction between Epichlorohydrin and Polysaccharides: Part 1. Syntheses of Some Model Substances with Non-Cyclic Substituents. *Carbohydr. Res.* **1994**, *262*, 213–221.
36. Hansen, M. F.; Morup, S. Estimation of Blocking Temperatures from ZFC/FC Curves. *J. Magn. Magn. Mater.* **1999**, *203*, 214–216.
37. Coffey, W. T.; Kalmykov, Y. P. Thermal Fluctuations of Magnetic Nanoparticles: Fifty Years after Brown. *J. Appl. Phys.* **2012**, 112.
38. Baleux, B. Colorimetric Determination of Nonionic Polyethylene Oxide Surfactants Using an Iodine−Iodide Solution. *C. R. Acad. Sci., Ser. C* **1972**, 279.
39. Abbott, A. J.; Nelsestuen, G. L. Association of a Protein with Membrane Vesicles at the Collisional Limit: Studies with Blood Coagulation Factor Va Light Chain Also Suggest Major Differences between Small and Large Unilamellar Vesicles. *Biochemistry* **1987**, *26*, 7994–8003.
40. Pedersen, M. B.; Zhou, X.; Larsen, E. K.; Sorensen, U. S.; Kjems, J.; Nygaard, J. V.; Nyengaard, J. R.; Meyer, R. L.; Boesen, T.; Vorup-Jensen, T. Curvature of Synthetic and Natural Surfaces Is an Important Target Feature in Classical Pathway Complement Activation. *J. Immunol.* **2010**, *184*, 1931–1945.
41. Goldstein, I. J.; Hollerman, C. E.; Smith, E. E. Protein-Carbohydrate Interaction. II. Inhibition Studies on the Interaction of Concanavalin A with Polysaccharides. *Biochemistry* **1965**, *4*, 876–883.
42. Smith, E. E.; Goldstein, I. J. Protein-Carbohydrate Interaction. V. Further Inhibition Studies Directed toward Defining the Stereochemical Requirements of the Reactive Sites of Concanavalin A. *Arch. Biochem. Biophys.* **1967**, *121*, 88–95.
43. Alexis, F.; Pridgen, E.; Molnar, L. K.; Farokhzad, O. C. Factors Affecting the Clearance and Biodistribution of Polymeric Nanoparticles. *Mol. Pharmaceutics* **2008**, *5*, 505–515.
44. Perrault, S. D.; Walkey, C.; Jennings, T.; Fischer, H. C.; Chan, W. C. Mediating Tumor Targeting Efficiency of Nanoparticles through Design. *Nano Lett.* **2009**, *9*, 1909–1915.
45. Moghimi, S. M.; Hunter, A. C.; Murray, J. C. Long-Circulating and Target-Specific Nanoparticles: Theory to Practice. *Pharmacol. Rev.* **2001**, *53*, 283–318.
46. Simberg, D.; Zhang, W. M.; Merkulov, S.; McCrae, K.; Park, J. H.; Sailor, M. J.; Ruoslahti, E. Contact Activation of Kallikrein-Kinin System by Superparamagnetic Iron Oxide Nanoparticles in Vitro and in Vivo. *J. Controlled Release* **2009**, *140*, 301–305.
47. Moghimi, S. M.; Hunter, A. C.; Andresen, T. L. Factors Controlling Nanoparticle Pharmacokinetics: An Integrated Analysis and Perspective. *Annu. Rev. Pharmacol. Toxicol.* **2012**, *52*, 481–503.
48. Moghimi, S. M.; Farhangrazi, Z. S. Nanomedicine and the Complement Paradigm. *Nanomed.: Nanotechnol., Biol., Med.* **2013**, *9*, 458–460.
49. Ricklin, D.; Hajishengallis, G.; Yang, K.; Lambris, J. D. Complement: A Key System for Immune Surveillance and Homeostasis. *Nat. Immunol.* **2010**, *11*, 785–797.
50. Brown, E. J. Complement Receptors, Adhesion, and Phagocytosis. *Infect. Agents Dis.* **1992**, *1*, 63–70.
51. Sengelov, H. Complement Receptors in Neutrophils. *Crit. Rev. Immunol.* **1995**, *15*, 107–131.
52. Peng, Q.; Li, K.; Sacks, S. H.; Zhou, W. The Role of Anaphylatoxins C3a and C5a in Regulating Innate and Adaptive Immune Responses. *Inflammation Allergy: Drug Targets* **2009**, *8*, 236–246.
53. Mestas, J.; Hughes, C. C. W. Of Mice and Not Men: Differences between Mouse and Human Immunology. *J. Immunol.* **2004**, *172*, 2731–2738.
54. Chao, Y.; Makale, M.; Karmali, P. P.; Sharikov, Y.; Tsigelny, I.; Merkulov, S.; Kesari, S.; Wrasidlo, W.; Ruoslahti, E.; Simberg, D. Recognition of Dextran-Superparamagnetic Iron Oxide Nanoparticle Conjugates (Feridex) via Macrophage Scavenger Receptor Charged Domains. *Bioconjugate Chem.* **2012**, *23*, 1003–1009.
55. Chao, Y.; Karmali, P. P.; Mukthavaram, R.; Kesari, S.; Kouznetsova, V. L.; Tsigelny, I. F.; Simberg, D. Direct Recognition of Superparamagnetic Nanocrystals by Macrophage Scavenger Receptor Sr-Ai. *ACS Nano* **2013**, *7*, 4289–4298.
56. Karmali, P. P.; Simberg, D. Interactions of Nanoparticles with Plasma Proteins: Implication on Clearance and Toxicity of Drug Delivery Systems. *Expert Opin. Drug Delivery* **2011**, *8*, 343–357.

57. Li, S. D.; Huang, L. Pharmacokinetics and Biodistribution of Nanoparticles. *Mol. Pharmaceutics* **2008**, *5*, 496–504.
58. Klibanov, A. L.; Maruyama, K.; Beckerleg, A. M.; Torchilin, V. P.; Huang, L. Activity of Amphipathic Poly(Ethylene Glycol) 5000 to Prolong the Circulation Time of Liposomes Depends on the Liposome Size and Is Unfavorable for Immunoliposome Binding to Target. *Biochim. Biophys. Acta* **1991**, *1062*, 142–148.
59. Duncanson, W. J.; Figa, M. A.; Hallock, K.; Zalipsky, S.; Hamilton, J. A.; Wong, J. Y. Targeted Binding of Pla Microparticles with Lipid-PEG-Tethered Ligands. *Biomaterials* **2007**, *28*, 4991–4999.
60. Cai, W.; Chen, X. Multimodality Molecular Imaging of Tumor Angiogenesis. *J. Nucl. Med.* **2008**, *49* (Suppl 2), 113S–28S.
61. Barrett, T.; Brechbiel, M.; Bernardo, M.; Choyke, P. L. MRI of Tumor Angiogenesis. *J. Magn. Reson. Imaging: JMRI* **2007**, *26*, 235–249.
62. Iagaru, A.; Chen, X.; Gambhir, S. S. Molecular Imaging Can Accelerate Anti-Angiogenic Drug Development and Testing. *Nat. Clin. Pract. Oncol.* **2007**, *4*, 556–557.
63. Thorek, D. L.; Tsourkas, A. Size, Charge and Concentration Dependent Uptake of Iron Oxide Particles by Non-Phagocytic Cells. *Biomaterials* **2008**, *29*, 3583–3590.
64. Schnell, M. A.; Hardy, C.; Hawley, M.; Propert, K. J.; Wilson, J. M. Effect of Blood Collection Technique in Mice on Clinical Pathology Parameters. *Human Gene Ther.* **2002**, *13*, 155–161.